Phase-locked photonic wire lasers by π coupling

Ali Khalatpour[1], John L. Reno[2] and Qing Hu [1,3]*

The term photonic wire laser is now widely used for lasers with transverse dimensions much smaller than the wavelength. As a result, a large fraction of the mode propagates outside the solid core. Here, we propose and demonstrate a scheme to form a coupled cavity by taking advantage of this unique feature of photonic wire lasers. In this scheme, we used quantum cascade lasers with antenna-coupled third-order distributed feedback grating as the platform. Inspired by the chemistry of hybridization, our scheme phase-locks multiple such lasers by π coupling. With the coupled-cavity laser, we demonstrated several performance metrics that are important for various applications in sensing and imaging: a continuous electrical tuning of ~10 GHz at ~3.8 THz (fractional tuning of ~0.26%), a good level of output power (~50–90 mW of continuous-wave power) and tight beam patterns (~10⁰ of beam divergence).

In photonic wire lasers[1–5], which are characterized as $w \ll \lambda$ (where w is the dimension of the cross-section and λ is the wavelength), a large fraction of the mode propagates outside the deep subwavelength core. As a result, the radiation properties of a wire laser can be efficiently manipulated by perturbing its lateral boundary condition, both electrically and geometrically. This unique feature was utilized in a tunable laser whose frequency could be changed by moving an object placed alongside the wire laser[6]. Achieving a tight beam pattern, single-frequency operation, and high output power at the same time in such lasers is a challenging task due to the deep subwavelength transverse dimensions. Moreover, in many applications, electrically tuning the laser frequency is crucial, in addition to high output power and tight beam pattern. For example, recent developments in quantum cascade laser (QCL) technology has enabled NASA to initiate the Galactic/Extragalactic ULDB Spectroscopic Terahertz Observatory (GUSTO)[7] that will measure emissions from the interstellar medium. Measurement of the neutral oxygen line (OI at 4.744 THz), which will provide important information on star formation, is at the heart of this mission[8,9]. The highest linear velocity of the interstellar medium in the Milky Way[10] is ~250 km s⁻¹ that will yield a Doppler shift of ±0.08%, corresponding to ±4 GHz at 4.744 THz. Hence, a local oscillator that can be electrically tuned over ~8 GHz will be essential for mapping the OI line over the entire Milky Way. Besides the importance for determining this specific spectral line, the frequency range of 1–5 THz is also rich with spectral fingerprints of many biochemical species. For instance, low-frequency vibrations of biotin (I) was investigated in the range 0.8–3.8 THz to better understand the conformational flexibility responsible for its bioactivity[11]. Applications in breast cancer imaging[12], skin cancer imaging[13], colon cancer imaging[14], brain imaging[15,16], identifying explosives[17], inspecting defects in airplanes[18] and identifying protein structures[19] have been demonstrated in the same frequency range. A terahertz (THz) imaging system based on a double heterodyne detection scheme[20] has yielded a signal-to-noise ratio of 110 dB. Such a large signal-to-noise ratio and the corresponding dynamic range will be useful in enhancing the imaging capability. In this scheme, the required output power is ~50 mW in continuous-wave (c.w.) operations that is not easily accessible and was achieved by using bulky far-infrared gas lasers. Therefore, achieving >8 GHz of electrical frequency tuning, a c.w.

output power >50 mW and good beam quality would be of great interest in various applications.

A significant attempt has been made to improve wire laser performance in the THz range in terms of output power and power efficiency, beam pattern, and frequency tunability. Recently, up to 1% wall-plug efficiency with ~16 mW of c.w. power and single-frequency operation by using a unidirectional antenna-coupled third-order distributed feedback grating (ADFB) has been demonstrated[21]. By using a new hybrid grating scheme that uses a superposition of second- and fourth-order Bragg gratings, peak power of 170 mW with a slope efficiency of 993 mW A⁻¹ is achieved[22]. In pulsed mode, peak THz output power up to 830 mW at 77 K and 1.35 W at 6 K is achieved using a THz quantum-cascade vertical-external-cavity surface-emitting laser[23]. In terms of beam quality, using the antenna-feedback method in THz QCLs, a single-mode THz QCL with a beam divergence as small as 4°×4° is demonstrated[24]. In terms of frequency tuning, by using piezoelectric actuators and an intra-cryostat cavity, tuning of ~260 GHz at a centre frequency of 3.3 THz is demonstrated with ~5 mW of c.w. power[25,26]. Frequency tuning of a THz quantum cascade wire laser over a broad range of ~330 GHz is demonstrated with a movable microelectromechanical systems (MEMS) side object (plunger) actuated by force[27] or electrical bias[28] to manipulate the transverse optical mode. For pure electrical tuning, it has been demonstrated[29] that a laser device based on a coupled cavity, in which two 'knobs' can be tuned by independently biasing the two devices, can achieve electrical tuning with a good range of ~4 GHz (within 50% of output power variation) and 0.7 mW of c.w. power. In microdisk lasers of small optical volume, a single whispering-gallery mode can in fact be current-tuned by ~30 GHz through gain pulling[30,31], although the output power changed significantly over the entire tuning range. In a recent work, an electrical tuning method for a THz QCL is developed based on detuned intersubband absorption in coupled metallic microcavities and ~4 GHz continuous frequency tuning is achived[32].

Thus far, no scheme has been devised to simultaneously achieve good beam quality, high c.w. output power and broad electrical frequency tuning. Here, we report the combination of all three desired features. Our scheme to achieve those performance metrics is based on phase locking of multiple wire lasers so that together they form a coupled cavity. A robust phase locking requires a strong coupling

¹Department of Electrical Engineering and Computer Science and Research Laboratory of Electronics, Massachusetts Institute of Technology, Cambridge, MA, USA. ²Sandia National Laboratories, Centre of Integrated Nanotechnologies, Albuquerque, NM, USA. ³Terahertz Technology Innovation Research Institute, and Shanghai Key Lab of Modern Optical System, University of Shanghai for Science and Technology, Shanghai, China. *e-mail: qhu@mit.edu
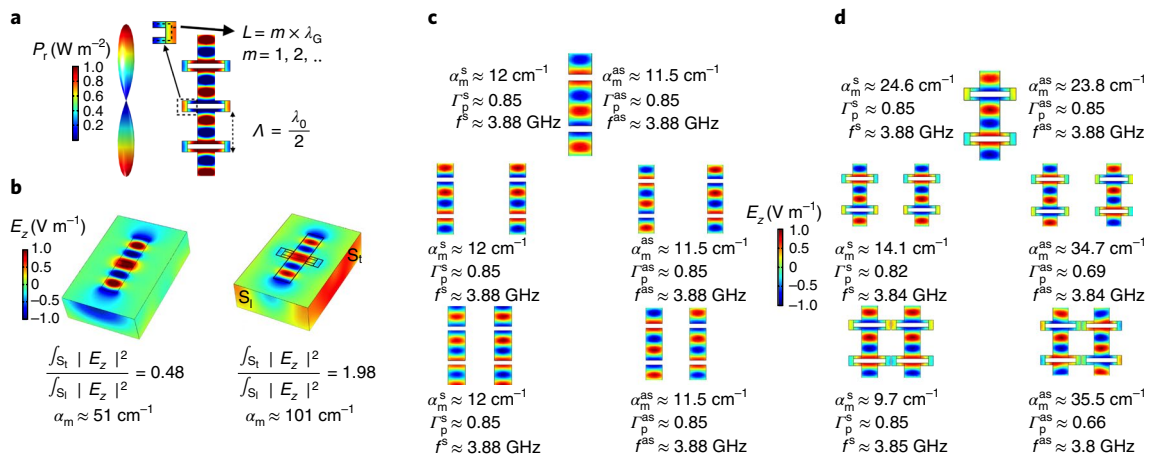
47

Fig. 1 | Full-wave simulations of DFB with and without antenna loop. a, Schematic of simulated fundamental mode and the beam pattern of an ADFB. Here, λ_0 is the free-space radiation wavelength, Λ is the grating periodicity and P_r is the far-field radiation intensity. **b**, Comparison between lateral intermediate zone radiation of a short (with two periods) third-order DFB with and without an antenna loop. **c**, Mirror loss α_m for a supermode formed in π-coupled DFBs (without the antenna loop) with a centre-to-centre distance $\approx 4\lambda_0$, λ_0, $\frac{\lambda_0}{2}$ (to save space, only one DFB is shown for the $4\lambda_0$ configuration). Superscript 's' represents the symmetric supermode and superscript 'as' the asymmetric supermode. **d**, Mirror loss α_m for a supermode formed in π-coupled ADFBs with a centre-to-centre distance of $\approx 4\lambda_0$, λ_0, $\frac{\lambda_0}{2}$. Simulations in **c** and **d** are performed for 10 periods. Here Γ is the mode confinement factor and f is the mode frequency.

among the individual lasers so that otherwise-independent oscillators are forced to oscillate in sync, even if they are biased quite differently. There are five major demonstrated coupling schemes to phase lock individual laser elements. Laser ridges can be coupled through exponentially decaying fields outside the high-refractive-index dielectric core[33] (evanescent-wave coupled), through the Talbot feedback from external reflectors[34,35] (diffraction-wave coupled), by connecting two ridges to one single-mode waveguide[36,37] (Y coupled), through lateral propagating waves[38–40] (leaky-wave coupled), or through mutual antenna coupling in the far field[41]. The evanescent-wave coupled scheme could be possibly used for two wire lasers with ridge waveguides. However, straight ridge waveguides have very divergent beam patterns and low extraction efficiency. Diffraction-wave coupling can also be used for wire lasers. However, this scheme requires an external component and delicate alignment. The scheme of Y-coupled ridge waveguides does not work well with distributed feedback grating (DFB) lasers, as the strong reflection in a DFB structure limits its facet coupling. Leaky-wave coupled schemes cannot be used effectively to couple DFB arrays as the radiation is mostly from radiation apertures and not from the end facets. For global antenna coupling[41], it is unclear if the phase locking can still be maintained if individual elements are biased at very different currents, which is required for frequency tuning at approximately constant optical power.

Here, we present a scheme for phase locking of several (≤ 5) wire lasers to form a coupled cavity, but with the main focus on the coupling of two for simplicity and clarity. We chose QCLs with ADFB as our platform[42]. ADFBs are a superior platform because of their tight beam patterns, high power and high wall-plug efficiency. Single-mode operation, high c.w. output power of ~16 mW, 1% wall-plug efficiency and tight beam patterns have already been demonstrated in this platform[21]. The schematic of a single ADFB is shown in Fig. 1a. When a perfect phase-matching condition is met, the modal index $n_{eff} = \frac{3\lambda_0}{2\Lambda} = 3$, the radiations from all the antenna loops are in phase along the DFB structure, resulting in a tight far-field beam pattern[42]. An antenna loop increases the radiation ('mirror') loss by increasing the effective surface area for the radiation aperture. At resonance, the phases of the electric field inside the gaps are the same on both sides of the gap, thus the antenna length

L should be equal to $m \times \lambda_G$, where m is a positive integer and λ_G is the wavelength in the antenna loop.

It should be noted that in an ADFB, the radiation is mostly from the antenna loop. Owing to negligible facet radiation, Y and diffraction grating coupling schemes are not applicable here. Since the antenna loop length is determined by the resonance condition, ADFB pairs are ~λ_G apart so the evanescent lateral coupling between the ridges is negligible. Since an ADFB with even only a few periods produces a tight beam pattern in the longitudinal direction, far-field coupling through mutual antenna coupling is also not applicable here as this scheme relies on a very divergent beam pattern from individual lasers. Our simulation shows that the fundamental DFB mode is largely confined longitudinally near the centre portion. This mode localization and negligible radiation from the facets limit the leaky-wave coupling[40].

Through this discussion, it can be inferred that phase locking of ADFBs requires a new coupling mechanism, which is the π coupling reported in this work. Although the mechanisms are different, the development of the π-coupling scheme in this work was inspired by π conjugation in chemistry. For a photonic wire laser, the radiation from each subwavelength aperture is divergent. A simulated radiation profile of a single-period third-order DFB with (ADFB) and without an antenna loop is shown in Fig. 1b. It can be observed that by attaching the antenna loop, not only does the mirror loss increase but also the lateral field distribution in the intermediate zone (~λ) is significantly enhanced. The quantitative treatment of lateral radiation is shown in Fig. 1b through the integration of the dominant component of the electric field (here E_z). The strong lateral field distribution opens up the possibility for the π coupling of two or even more ADFBs. Since the coupling exists between all in-phase antenna radiation gaps, this scheme will be far more effective compared with earlier schemes utilizing the facet radiation. The same cannot be said for a third-order DFB without the antenna loop. Even though the beam from the radiating aperture is divergent, there is no strong coupling to an adjacent gap through π coupling.

Since a strong coupling will reduce the mirror loss α_m for the coupled cavities[41], it can be used to quantify the coupling strength. As shown in Fig. 1c, α_m for the third-order DFB without the antenna loop[43] is not changed significantly as those DFBs are brought close
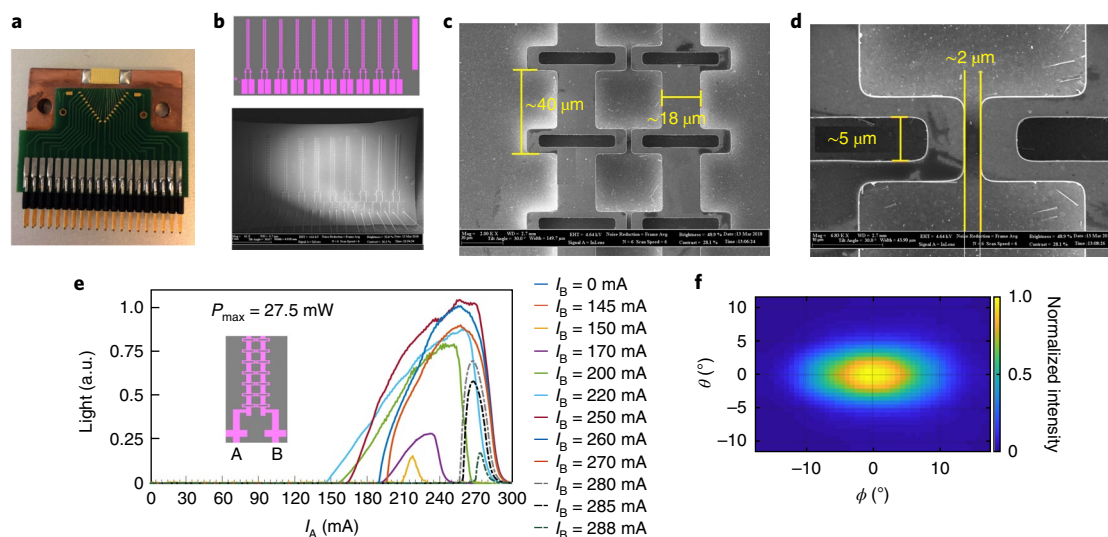
Fig. 2 | Experimental verification of π-coupled ADFB. a, Electronic chip for simultaneous independent biasing. **b**, A fabricated die with 10 pairs of π-coupled ADFBs. Top: schematic. Bottom: scanning electron microscopy (SEM) image. **c**, Three periods are shown (from a total 35 periods) in the fabricated π-coupled ADFB. **d**, Magnified SEM image of the gap between the antenna loops. **e**, Light–current curves. P_{max} is the maximum c.w. output power of the π-coupled ADFB. **f**, Beam pattern of π-coupled ADFB. Here, the laser is located along the z axis in a spherical coordinate system.
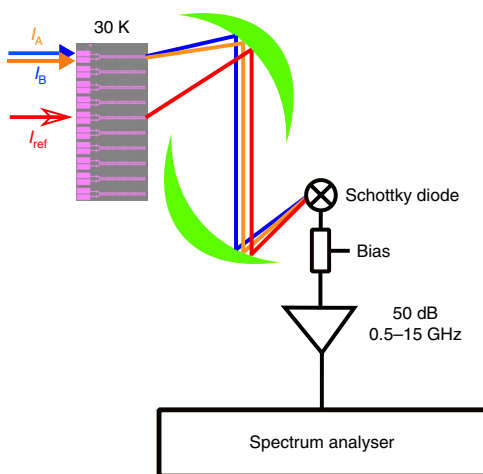

Fig. 3 | Experimental set-up for measuring frequency difference with kHz resolution. Experimental set-up for heterodyne mixing to measure a possible frequency difference between π-coupled ADFBs, and later to measure the frequency tuning with high resolutions (~1 kHz). Here I_{ref} is current bias of the reference laser.

to each other, indicating a negligible π-coupling between the two. In addition, for very closely spaced cavities the asymmetric mode has a lower radiation loss and thus it will be the lasing mode, as it has a quadrupole moment with a lower radiation loss than a dipole moment. On the other hand, as shown in Fig. 1d, α_m for ADFBs is significantly reduced as they are brought closer to each other due to a strong π-coupling of the in-phase aperture fields. We further note that the cavities are decoupled for distances more than four wavelengths, suggesting that the coupling mechanism is not strong in the far field. Even at the closest distance between the antenna loops, the two ridges are ~λ_G apart so evanescent wave coupling between the ridges is negligible, but α_m is reduced by ~60% indicating a strong coupling. Also, we cannot characterize this as the leaky-wave coupling as there is no complex wave vector in the lateral direction (no lossy guided mode in the lateral direction).

To explain the selectivity between the symmetric and asymmetric modes, we emphasize that the shortest antenna loop length is λ_G at resonance, so that the tip of two parallel antenna arms is $\frac{\lambda_G}{2}$ apart from the edge of the gap, producing a 180° phase shift compared with the field in the gap. For an isolated ADFB, the field in the gap is approximately constant and $E_{gap} \approx E_{max}$, and the field near the tip should be $E_{tip} \sim -E_{max}$ (but smaller in magnitude). Clearly, such a field distribution is totally compatible with that in the symmetric supermode, resulting in a minimum mode distortion. As can be seen in Fig. 1d, the mode profile for the symmetric supermode resembles closely with that in an isolated ADFB. The additional intracavity coupling reduces the mirror loss from that of an isolated ADFB. For the asymmetric supermode, however, the field at the centre line of the two ADFBs is identical to be zero. Thus, when the two tips are brought together, the field at the tip should also be zero, which forces the field at the gap edge to be approximately equal to zero. This field distribution is quite different from an isolated ADFB, causing a significant mode distortion and consequently a lower mode confinement factor, as shown in Fig. 1d. The lower confinement factor yields a higher mirror loss. In a simplistic view, an asymmetric mode resembles a higher-order lateral mode in a single ridge that tends to have a higher lasing threshold. The quantitative treatment of the mode confinement factor for symmetric and asymmetric modes is given in Fig. 1d. As shown, the mode confinement factor for the asymmetric mode is decreased at a smaller distance between the ADFBs, indicating a higher level of mode distortion. As a result, the lasing threshold for the symmetric mode becomes much lower than the asymmetric mode due to its lower mirror loss and higher mode confinement factor.

Results and discussion

To demonstrate the phase locking in π-coupled ADFBs, we fabricated an array of π-coupled ADFBs. A schematic of the array along with several geometry parameters are shown in Fig. 2. Each array has 10 pairs of π-coupled ADFBs. The antenna loop length is varied from one pair to another to adjust the resonance condition. The distance between the pairs is designed to be sufficiently large to avoid inter-pair coupling. Considering the fabrication resolution, the gap between the antenna loops in an ADFB pair is set to $\frac{\lambda_0}{40} = 2$ μm. The size of the gap within the antenna loop is 5.5 μm to ensure a high

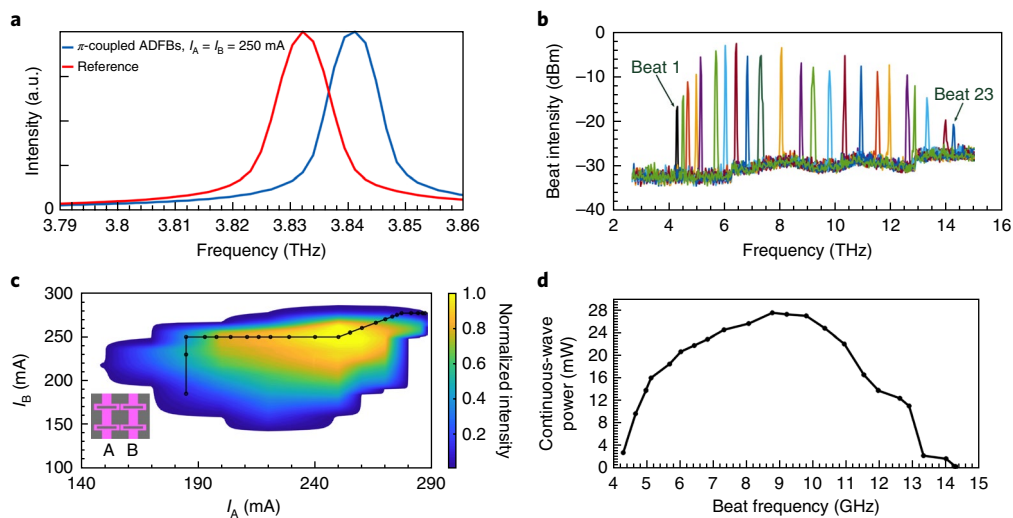**Fig. 4 | Frequency tuning of π-coupled ADFBs. a**, Measured frequencies from an FTIR spectrometer. **b**, The frequency difference between the π-coupled ADFBs and the reference measured using a Schottky diode mixer. **c**, A 2D path for the different bias levels based on the dynamic range and output power consideration. **d**, Output power versus the beat frequency.
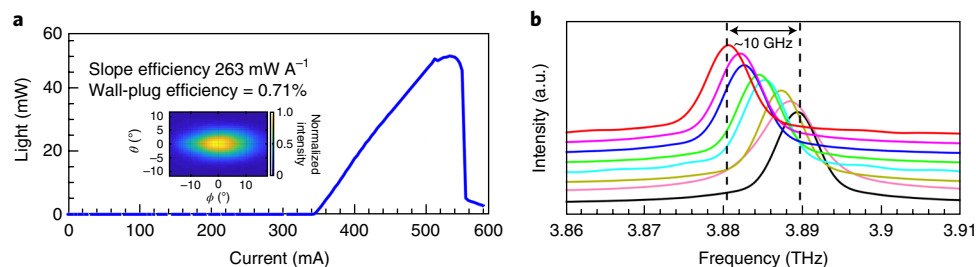

Fig. 5 | Result of a π-coupled ADFB optimized for output power. a, $I_A = I_B$ c.w. light–current curve and beam pattern (inset). **b**, Spectra taken with an FTIR spectrometer on the linear part of the curve in **a**.

mirror loss α_m. Based on the simulations, α_m for the supermode is 40% of that of a single ADFB and predicted to be 6 cm^{-1} for the symmetric supermode. The centre frequency of π-coupled ADFBs in this chip is designed to be around 3 GHz apart from the adjacent pair (by simply increasing the antenna loop length by ~4%, monotonically decreasing frequency shift can be achieved). The measurement results are shown in Fig. 2e,f. The observed interdependence of current thresholds and a single-lobe beam pattern is strong evidence for a symmetric supermode. In particular, no lasing was observed if one ADFB was unbiased, suggesting a significant loss in a cold cavity and a strong coupling between the two. When both are biased, as the bias for one ADFB is increased, the lasing threshold for the bias of the other ADFB decreased, indicating that the total gain increased in the coupled cavity.

To measure a possible frequency offset between the two π-coupled ADFBs, we prepared the experimental set-up shown in Fig. 3. The reference laser shown in Fig. 3 is turned off for this measurement. This scheme enabled us to measure the frequency separation up to 20 GHz with ~kHz resolution using a spectrum analyser. In this set-up, the radiation from π-coupled ADFBs is focused on a Schottky diode mixer. The horn antenna integrated with the mixer has an accepting aperture with dimensions ~500 μm × 500 μm. To achieve a high signal-to-noise ratio on the mixer, two off-axis paraboloid mirrors are used to focus the beam onto the horn antenna aperture. The DC monitor port of the mixer is connected to a lock-in amplifier for the optical alignment. The radio-frequency port is connected to a spectrum analyser through a 50-dB low-noise amplifier.

We have observed single-mode operation (without observing any beatnote up to 20 GHz with kHz resolution) in the entire bias range shown in Fig. 2e. This indicates that the π-coupling scheme is strong enough to maintain a robust phase locking throughout the entire bias range.

The main motivation for phase-locked ADFBs with separate biases is to achieve frequency tuning with approximately constant output power. Varying the relative bias of π-coupled ADFBs changes the gain profile. Deducing from the Kramers–Kronig relation[44], this variation causes changes in the refractive index that produce a slight frequency shift. In more technical terms, this is referred to as the mode-pulling effect, which is produced by the blue-shift of the underlying gain profile with applied bias, and the associated change in the refractive index shifts the resonance frequency[45,46]. Based on this change of refractive index, π-coupled ADFBs can produce continuous frequency tuning with a greater tuning range than a single device as they can act like a master-slave oscillator.

Using the same set-up shown in Fig. 3, we used another π-coupled ADFB on the same die as the reference (we performed a separate measurement confirming its single-mode operation) that was three pairs away from the π-coupled ADFB under investigation. The distant pair was chosen to ensure a sufficient separation of centre frequencies and to avoid possible local heating. To rule out thermal tuning, the cold stage was stabilized at 30 K using a PID temperature controller. The frequency of the reference and the π-coupled ADFBs measured by Fourier-transform infrared (FTIR) spectroscopy and their relative positions on the die are shown in Fig. 4a.
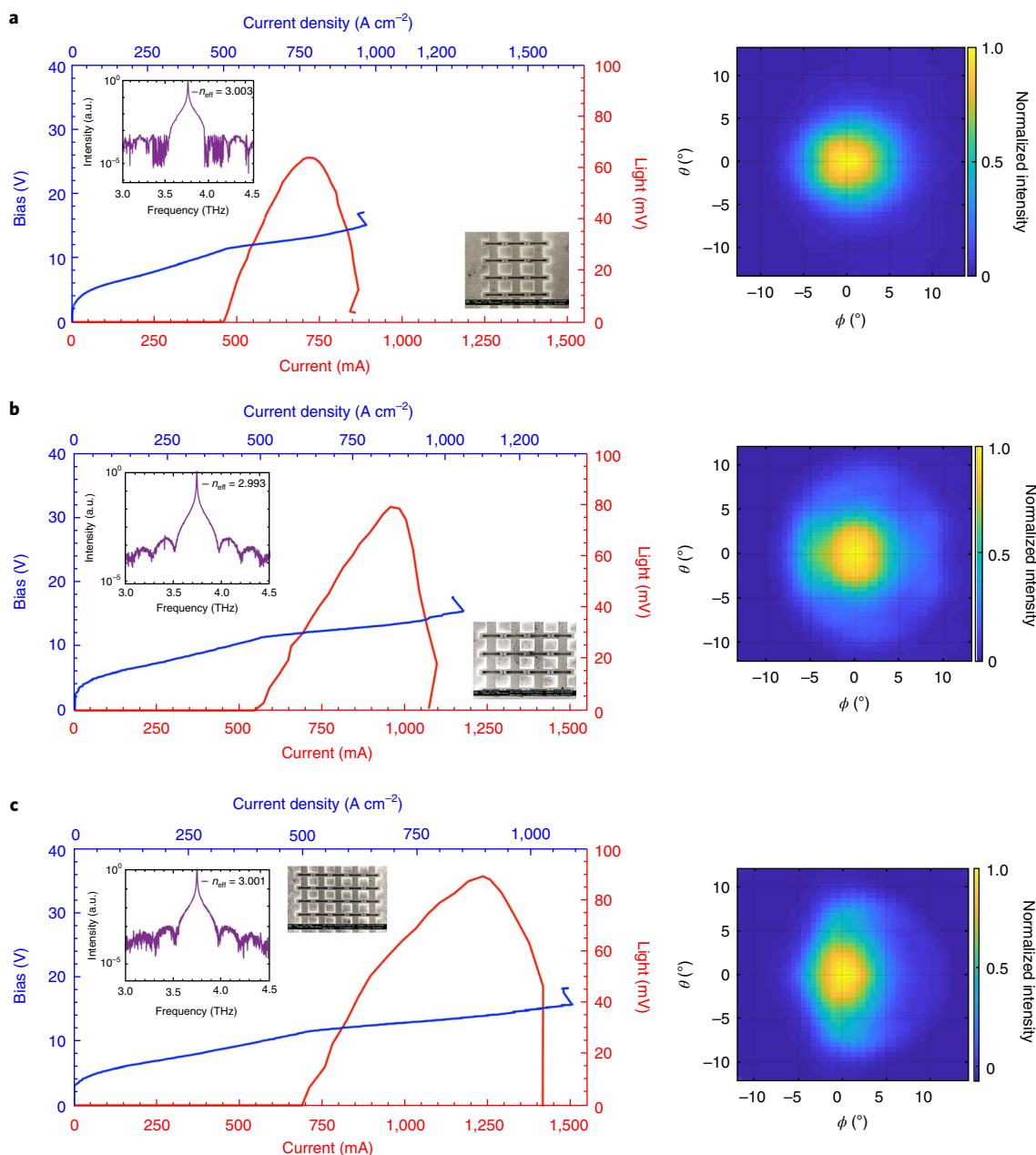
Fig. 6 | Versatility of the π-coupled scheme for higher numbers of ADFBs. a–c, Spectra, SEM images, *L–I–V* curves and beam patterns for three π-coupled ADFBs (**a**), four π-coupled ADFBs (**b**) and five π-coupled ADFBs (**c**).

Figure 4b shows the beat frequency along the current path shown in Fig. 4c (black line, which was aimed for minimum power variation and highest dynamic range). Figure 4d shows the output power of the supermode at corresponding points. We observed ~10 GHz of frequency tuning with a maximum c.w. output power of ~27 mW; 7 GHz of this frequency change is within 50% power change. Even though we only included a few points in the graph, we observed a complete continuous change on the spectral analyser as we changed the biases along the indicated path. No mode hopping was observed. It is worth mentioning that since all off-centred π-coupled ADFBs are tested and proved to be single mode, one can design the centre frequency of each π-coupled ADFB to be about 10 GHz (for this gain medium) apart. In this case, by electrically switching between the π-coupled ADFBs, a much greater continuous tuning range can be achieved.

As shown in Fig. 1d, the supermode in a π-coupled ADFB has significantly lower mirror loss than the uncoupled counterpart. It is well known that the output power from a laser is proportional to $\frac{\alpha_m}{\alpha_m + \alpha_w}$, where α_m is the mirror (radiation) loss and α_w is the waveguide loss[47]. For a maximum output power, $\alpha_m \approx \alpha_w$. In our case, the measured[48] $\alpha_w \sim 15 \, \text{cm}^{-1}$. Therefore, one can design individual ADFBs with much higher mirror loss so that the π-coupled ADFBs have optimum mirror loss for the symmetric supermode. Here we used another pair of ADFBs and increased the antenna gap size to 6 μm. Simulations show an 8 cm^{-1} mirror loss for the symmetric supermode. The measurement results are shown in Fig. 5. Measurements confirm a single-mode frequency at 3.87 GHz with ~10 GHz of frequency tuning, ~50 mW of c.w. power and a high-quality beam pattern. The wall-plug efficiency was measured to be 0.71% and the slope efficiency was 263 mW A^{-1}. Here, having

already proved the continuous nature of frequency tuning, we simply measured the spectra with FTIR spectroscopy.

To demonstrate the versatility of the π-coupled phase-locking mechanism, we designed and fabricated π-coupled ADFBs with more than two ADFBs. By coupling more ADFBs, even higher power levels can be achieved; and, in principle, with more knobs to turn, a better performance (for example, less power variation over the entire frequency tuning range) can be achieved. Figure 6 shows the results for π-coupled 3, 4 and 5 ADFBs with each having 35 periods and 5.5-µm slot gap size. For fabrication and operation simplicity, all the ADFBs were biased together using one bonding pad. The single-mode spectra and single-lobe beam pattern clearly show that these ADFBs are phase locked. As the number of ADFBs increased, the lateral beam pattern became narrower, as expected. The total current for the coupled ADFBs scales linearly with the number of ADFBs. However, the output power does not increase linearly since the mirror loss decreases with an increasing number of coupled ADFBs. It is worth noting that the effective index for the coupled array is closer to 3 than individual elements. By increasing the number of coupled ADFBs, the radiation loss decreases, which increases the effective modal index and brings it closer to the ideal value for perfect phase matching ($n_{eff} = 3$). Such phase matching is difficult to achieve for a high-power single ADFB since it will require a larger slot gap size that yields $n_{eff} < 3$.

In conclusion, we have demonstrated a π-coupled scheme to phase lock 2, 3, 4 and 5 ADFBs. The coupling mechanism is sufficiently strong to maintain a robust phase locking at all biases. Tight beam patterns ($\sim 10° \times 15°$), ~ 50 mW for two π-coupled ADFBs (~ 90 mW for 5 π-coupled ADFBs with $\sim 6° \times 8°$ half power beam width), and ~ 10 GHz of continuous electrical frequency tuning is demonstrated at 30 K. With the 20-pins connector shown in Fig. 2a (which is by no means the upper limit), one can envision to bias 10 pairs of ADFBs with a frequency separation of ~ 10 GHz by varying the lengths of the antenna loops and the periods of the DFB structure. With each pair of ADFBs tunable by ~ 10 GHz, the whole chip can be electrically tuned continuously over ~ 100 GHz. Such broad and continuous electrical tuning will be highly desirable in sensing and imaging.

Online content

Any methods, additional references, Nature Research reporting summaries, source data, statements of data availability and associated accession codes are available at https://doi.org/10.1038/s41566-018-0307-0.

References

1. Hill, M. T. et al. Lasing in metallic-coated nanocavities. *Nat. Photon.* **1**, 589–594 (2007).
2. Noginov, M. et al. Demonstration of a spaser-based nanolaser. *Nature* **460**, 1110–1112 (2009).
3. Oulton, R. F. et al. Plasmon lasers at deep subwavelength scale. *Nature* **461**, 629–633 (2009).
4. Zhang, J. et al. Photonic-wire laser. *Phys. Rev. Lett.* **75**, 2678–2681 (1995).
5. Hill, M. T. & Gather, M. C. Advances in small lasers. *Nat. Photon.* **8**, 908–918 (2014).
6. Qin, Q., Williams, B. S., Kumar, S., Reno, J. L. & Hu, Q. Tuning a terahertz wire laser. *Nat. Photon.* **3**, 732–737 (2009).
7. Walker, C. K. et al. GUSTO: Gal/Xgal U/LDB Spectroscopic-Stratospheric Terahertz Observatory. In *Am. Astron. Soc. Meeting Abstracts* Vol. 231 (2018).
8. Kloosterman, J. L. et al. Hot electron bolometer heterodyne receiver with a 4.7-THz quantum cascade laser as a local oscillator. *Appl. Phys. Lett.* **102**, 011123 (2013).
9. Mirzaei, B. et al. 8-beam local oscillator array at 4.7 THz generated by a phase grating and a quantum cascade laser. *Opt. Express* **25**, 29587–29596 (2017).
10. Pikel'ner, S. Structure and dynamics of the interstellar medium. *Annu. Rev. Astron. Astrophys.* **6**, 165–194 (1968).
11. Korter, T. & Plusquellic, D. F. Continuous-wave terahertz spectroscopy of biotin: vibrational anharmonicity in the far-infrared. *Chem. Phys. Lett.* **385**, 45–51 (2004).
12. Fitzgerald, A. et al. Terahertz imaging of breast cancer, a feasibility study. In *Conf. Digest of the 2004 Joint 29th Int. Conf. Infrared and Millimeter Waves and 12th Int. Conf. Terahertz Electron.* 823–824 (IEEE, 2004).
13. Rahman, A., Rahman, A. K. & Rao, B. Early detection of skin cancer via terahertz spectral profiling and 3D imaging. *Biosens. Bioelectron.* **82**, 64–70 (2016).
14. Eadie, L. H., Reid, C. B., Fitzgerald, A. J. & Wallace, V. P. Optimizing multi-dimensional terahertz imaging analysis for colon cancer diagnosis. *Expert Syst. Appl.* **40**, 2043–2050 (2013).
15. Darmo, J. et al. Imaging with a terahertz quantum cascade laser. *Opt. Express* **12**, 1879–1884 (2004).
16. Bakopoulos, P. et al. A tunable continuous wave (cw) and short-pulse optical source for THz brain imaging applications. *Meas. Sci. Technol.* **20**, 104001 (2009).
17. Shen, Y. et al. Detection and identification of explosives using terahertz pulsed spectroscopic imaging. *Appl. Phys. Lett.* **86**, 241116 (2005).
18. Duling, I. & Zimdars, D. Terahertz imaging: revealing hidden defects. *Nat. Photon.* **3**, 630–632 (2009).
19. Ogawa, Y., Hayashi, S., Oikawa, M., Otani, C. & Kawase, K. Interference terahertz label-free imaging for protein detection on a membrane. *Opt. Express* **16**, 22083–22089 (2008).
20. Siegel, P. H. & Dengler, R. J. Applications & early results from THz heterodyne imaging at 119/spl mu/m. In *Conf. Digest of the 2004 Joint 29th Int. Conf. Infrared and Millimeter Waves and 12th Int. Conf. Terahertz Electron.* 555–556 (IEEE, 2004).
21. Khalatpour, A., Reno, J. L., Kherani, N. P. & Hu, Q. Unidirectional photonic wire laser. *Nat. Photon.* **11**, 555–559 (2017).
22. Jin, Y. et al. High power surface emitting terahertz laser with hybrid second- and fourth-order Bragg gratings. *Nat. Commun.* **9**, 1407 (2018).
23. Curwen, C. A., Reno, J. L. & Williams, B. S. Terahertz quantum cascade VECSEL with watt-level output power. *Appl. Phys. Lett.* **113**, 011104 (2018).
24. Wu, C., Khanal, S., Reno, J. L. & Kumar, S. Terahertz plasmonic laser radiating in an ultra-narrow beam. *Optica* **3**, 734–740 (2016).
25. Curwen, C. A., Xu, L., Reno, J. L., Itoh, T. & Williams, B. S. Broadband continuous tuning of a THz quantum-cascade VECSEL. In *CLEO* paper STh4O–2 (OSA, 2017).
26. Xu, L. et al. Terahertz metasurface quantum-cascade VECSELs: theory and performance. *IEEE J. Sel. Top. Quantum Electron.* **23**, 1200512 (2017).
27. Qin, Q., Reno, J. L. & Hu, Q. MEMS-based tunable terahertz wire-laser over 330 GHz. *Opt. Lett.* **36**, 692–694 (2011).
28. Han, N. et al. Broadband all-electronically tunable MEMS terahertz quantum cascade lasers. *Opt. Lett.* **39**, 3480–3483 (2014).
29. Turčinková, D., Amanti, M. I., Scalari, G., Beck, M. & Faist, J. Electrically tunable terahertz quantum cascade lasers based on a two-sections interdigitated distributed feedback cavity. *Appl. Phys. Lett.* **106**, 131107 (2015).
30. Dunbar, L. A. et al. Small optical volume terahertz emitting microdisk quantum cascade lasers. *Appl. Phys. Lett.* **90**, 141114 (2007).
31. Zhang, H., Scalari, G., Faist, J., Dunbar, L. A. & Houdré, R. Design and fabrication technology for high performance electrical pumped terahertz photonic crystal band edge lasers with complete photonic band gap. *J. Appl. Phys.* **108**, 093104 (2010).
32. Zhao, L., Khanal, S., Gao, L., Reno, J. L. & Kumar, S. Electrical tuning of single-mode terahertz quantum-cascade lasers operating at high temperatures. In *2016 IEEE Photon. Conf.* 76–77 (IEEE, 2016).
33. Ackley, D. Single longitudinal mode operation of high power multiple-stripe injection lasers. *Appl. Phys. Lett.* **42**, 152–154 (1983).
34. Katz, J., Margalit, S. & Yariv, A. Diffraction coupled phase-locked semiconductor laser array. *Appl. Phys. Lett.* **42**, 554–556 (1983).
35. Brunner, D. & Fischer, I. Reconfigurable semiconductor laser networks based on diffractive coupling. *Opt. Lett.* **40**, 3854–3857 (2015).
36. Chen, K.-L. & Wang, S. Single-lobe symmetric coupled laser arrays. *Electron. Lett.* **21**, 347–349 (1985).
37. Streifer, W., Welch, D., Cross, P. & Scifres, D. Y-junction semiconductor laser arrays: part I–theory. *IEEE J. Quantum Electron.* **23**, 744–751 (1987).
38. Botez, D. & Peterson, G. Modes of phase-locked diode-laser arrays of closely spaced antiguides. *Electron. Lett.* **24**, 1042–1044 (1988).
39. Botez, D. High-power monolithic phase-locked arrays of antiguided semiconductor diode lasers. In *IEE Proc. J. Optoelectron.* **139**, 14–23 (IEE, 1992).
40. Kao, T.-Y., Hu, Q. & Reno, J. L. Phase-locked arrays of surface-emitting terahertz quantum-cascade lasers. *Appl. Phys. Lett.* **96**, 101106 (2010).
41. Kao, T.-Y., Reno, J. L. & Hu, Q. Phase-locked laser arrays through global antenna mutual coupling. *Nat. Photon.* **10**, 541–546 (2016).
42. Kao, T.-Y., Cai, X., Lee, A. W., Reno, J. L. & Hu, Q. Antenna coupled photonic wire lasers. *Opt. Express* **23**, 17091–17100 (2015).

43. Amanti, M., Fischer, M., Scalari, G., Beck, M. & Faist, J. Low-divergence single-mode terahertz quantum cascade laser. *Nat. Photon.* **3**, 586–590 (2009).
44. Roessler, D. Kramers-Kronig analysis of reflection data. *Br. J. Appl. Phys.* **16**, 1119–1123 (1965).
45. Beverini, N. et al. Frequency characterization of a terahertz quantum-cascade laser. *IEEE Trans. Instrum. Meas.* **56**, 262–265 (2007).
46. Fasching, G. et al. Subwavelength microdisk and microring terahertz quantum-cascade lasers. *IEEE J. Quantum Electron.* **43**, 687–697 (2007).
47. Faist, J. Wallplug efficiency of quantum cascade lasers: critical parameters and fundamental limits. *Appl. Phys. Lett.* **90**, 253512 (2007).
48. Burghoff, D. et al. A terahertz pulse emitter monolithically integrated with a quantum cascade laser. *Appl. Phys. Lett.* **98**, 061112 (2011).

Acknowledgements

Author contributions

A.K. conceived the idea, strategy, designed and fabricated the devices, performed the measurements and analysis, and wrote the manuscript. J.L.R. performed the molecular-beam epitaxy growth. All the work was done under the supervision of Q.H.

Competing interests

The authors declare no competing interests.

Additional information

Supplementary information is available for this paper at https://doi.org/10.1038/s41566-018-0307-0.

Reprints and permissions information is available at www.nature.com/reprints.

Correspondence and requests for materials should be addressed to Q.H.

Publisher's note: Springer Nature remains neutral with regard to jurisdictional claims in published maps and institutional affiliations.

Methods

Finite-element simulations. The simulations were carried out using COMSOL Multiphysics version 5.3. Material loss was not considered and the relative permittivity of GaAs was set to be 13. The top and bottom contacts were modelled as a perfect electric conductor. The power confinement factor was calculated in the simulations using $\dfrac{\iiint_A W_e \, dv}{\iiint_V W_e \, dv}$ in which W_e is the electric field energy density, and A and V refer to the active medium and the calculation domain volumes, respectively. The dominant electric field component in our structures is normal to the top and bottom plates and W_e is mainly from the z component of the electric field. The mirror loss was calculated from the imaginary part of the complex eigen frequency(f_i) using $\alpha_m = 4\pi n_r \dfrac{f_i}{c}$, where c is the speed of light and n_r is the real part of the GaAs refractive index that was set to 3.6.

Active gain medium. OWI210H is a three-quantum well GaAs/Al$_{0.15}$Ga$_{0.85}$As THz QCL[49]. It has a highly diagonal radiative transition (oscillator strength ~0.2) and a large injector anti-crossing (~1.7–2.0 meV). The 3D carrier concentration is 2.6×10^{15}. Pulse-mode maximum lasing temperature and emission frequency are ~170 K and ~3.8 THz, respectively. Average doping was verified using secondary ion mass spectroscopy (SIMS) performed by Evans Analytical Group.

Light–current–voltage and spectrum measurements. For pulsed light–current–voltage measurements and c.w. measurements, the lasers were operated at a temperature of 30 K. The relative optical power was measured with a QMC pyroelectric detector and mechanically chopped at 100 Hz. Spectra were measured using a Fourier transform infrared spectrometer (FTIR; model Thermo Nicolet 6700) with an internal deuterated tri-glycine sulfate (DTGS) detector.

Absolute power measurement. The relative power measured from the pyroelectric detector was calibrated using a Thomas Keating absolute THz power meter at a 30 Hz mechanical chopping frequency without any focusing optics between the laser and the power meter except a high-density polyethylene window on the cryostat. The laser under test was operated in c.w. at a temperature of 30 K inside a Cryomech Pulse tube cryo refrigerator (model PT 810). The maximum lasing temperature was 121 K for the pulsed and 75 K for the c.w. operations. Power dropped to 50% at 70 K for the pulsed mode and 57 K for the c.w. mode.

Beam pattern measurement. Far-field beam patterns were measured with a pyroelectric detector mounted on a 2D motorized scanning stage that was placed at 10 cm from the lasers scanning between ±30° for both directions without any optics between the laser and the detector. The laser was operated near the peak power in pulsed mode with 10% duty cycle and electronically chopped at 100 Hz.

Data availability

The data that support the plots within this paper and other finding of this study are available from the corresponding author upon reasonable request.

References

49. Chan, C. W. I., Albo, A., Hu, Q. & Reno, J. L. Tradeoffs between oscillator strength and lifetime in terahertz quantum cascade lasers. *Appl. Phys. Lett.* **109**, 201104 (2016).

In the format provided by the authors and unedited.

Phase-locked photonic wire lasers by π coupling

Ali Khalatpour[1], John L. Reno[2] and Qing Hu [ID][1,3]*

[1]Department of Electrical Engineering and Computer Science and Research Laboratory of Electronics, Massachusetts Institute of Technology, Cambridge, MA, USA. [2]Sandia National Laboratories, Centre of Integrated Nanotechnologies, Albuquerque, NM, USA. [3]Terahertz Technology Innovation Research Institute, and Shanghai Key Lab of Modern Optical System, University of Shanghai for Science and Technology, Shanghai, China. *e-mail: qhu@mit.edu

Beam patterns for symmetric and asymmetric modes

To emphasize the importance of mode selectivity between symmetric and asymmetric supermodes, Figure S1 shows the simulated difference between the far-field beam patterns of the asymmetric and symmetric supermodes. As expected, the dipole moment cancels out for an asymmetric mode and the quadrupole beam pattern appears. Without a mechanism to increase the mode selectivity, the asymmetric mode will be the lasing mode due to a smaller mirror loss.
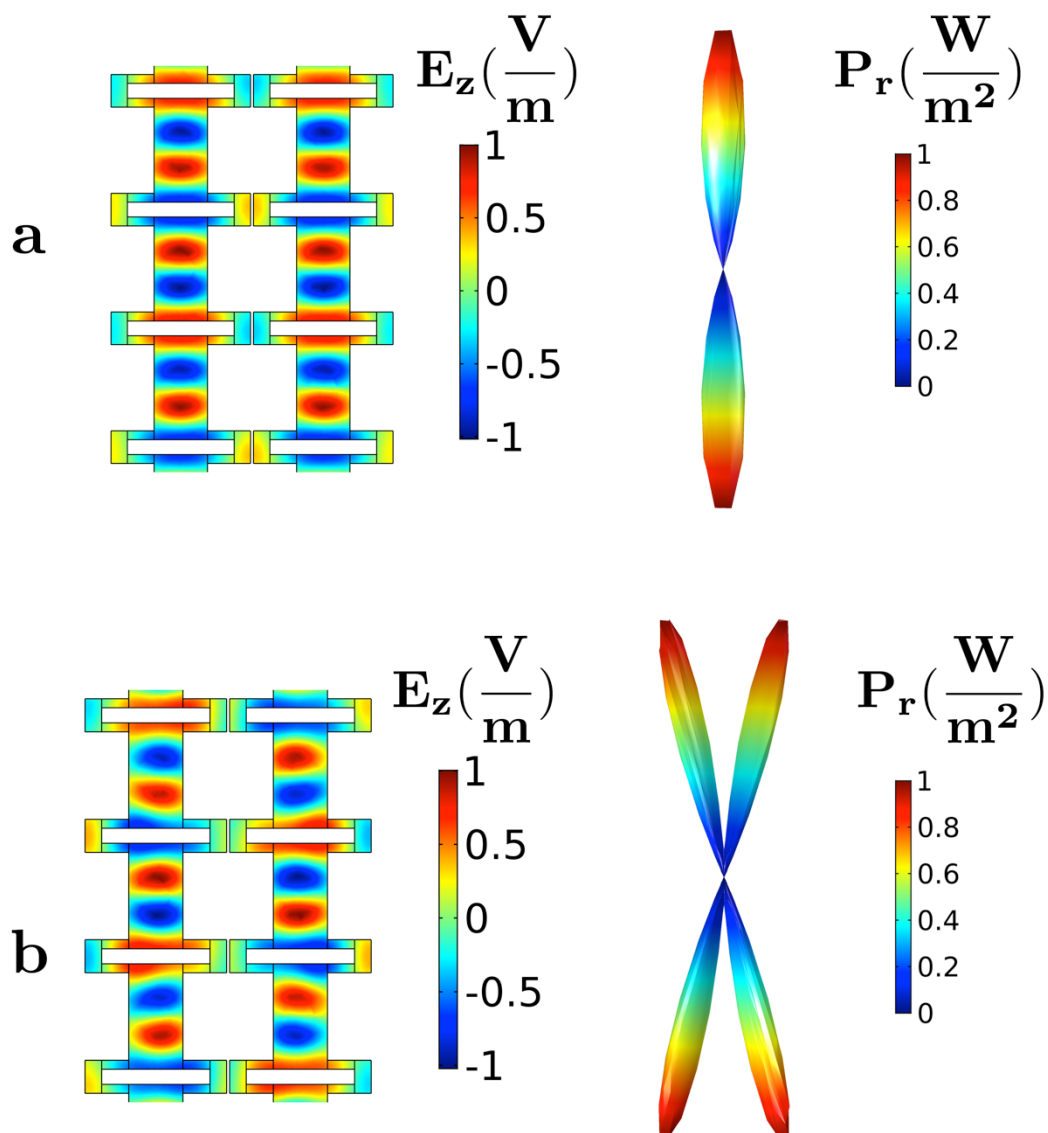

Figure S1: Comparison between the far field beam patterns for a, symmetric and b, asymmetric supermode of a π-coupled ADFBs.

Simulation for semi-infinite multiple π-coupled ADFBs

Using perfect electric (for asymmetric mode) and perfect magnetic boundary conditions (for symmetric mode), a relatively simple but sufficiently accurate simulation for an infinite number π-coupled ADFBs can be performed (since the dominant field component is tangent to those planes). By using these boundary conditions, the combined image fields resemble infinity in the lateral direction. The simulation results are shown in figure S2. There are 35 periods. Antenna length is set to be 9 μm and the antenna loop tips are 5.5-μm in thickness. The power confinement factor is smaller for asymmetric mode indicating a greater mode distortion from that of an isolated ADFB due to the perfect electric conductor boundary condition (the image current resembles neighbor ADFBs)
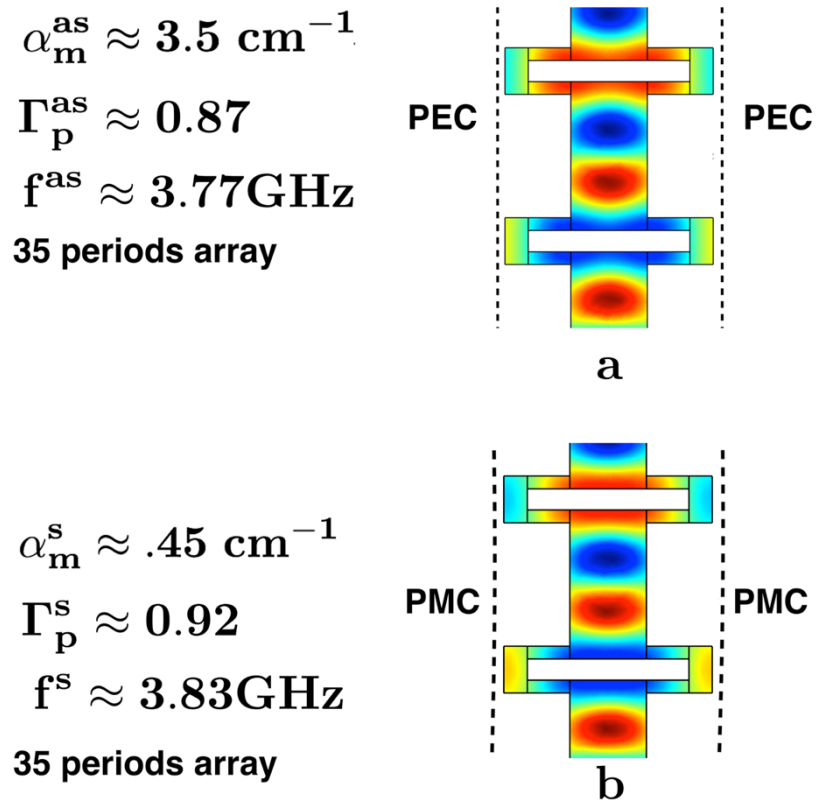
$$\alpha_m^{as} \approx 3.5 \text{ cm}^{-1}$$
$$\Gamma_p^{as} \approx 0.87$$
$$f^{as} \approx 3.77 \text{GHz}$$
35 periods array

PEC   PEC

a

$$\alpha_m^{s} \approx .45 \text{ cm}^{-1}$$
$$\Gamma_p^{s} \approx 0.92$$
$$f^{s} \approx 3.83 \text{GHz}$$
35 periods array

PMC   PMC

b

Figure S2: Comparison between the symmetric and asymmetric modes of an infinite stage π-coupled ADFBs

Comparison with a Fabry-Perot and a single ADFB device

It is informative to compare the tuning range of a π-coupled ADFBs to a single ADFB. Figure S3 shows the characteristics of a single ADFB with its corresponding bias tuning range along with a Fabry Perot (FP) device. We can see that the tuning range for a single ADFB is about 6 GHz. The lower J_{max} in DFB compared to a FP device is a result of high mirror loss, which causes a higher J_{th} and thus a reduced dynamic range in a highly diagonal structure[1]. Both ADFB and FP devices are fabricated from the same gain medium.
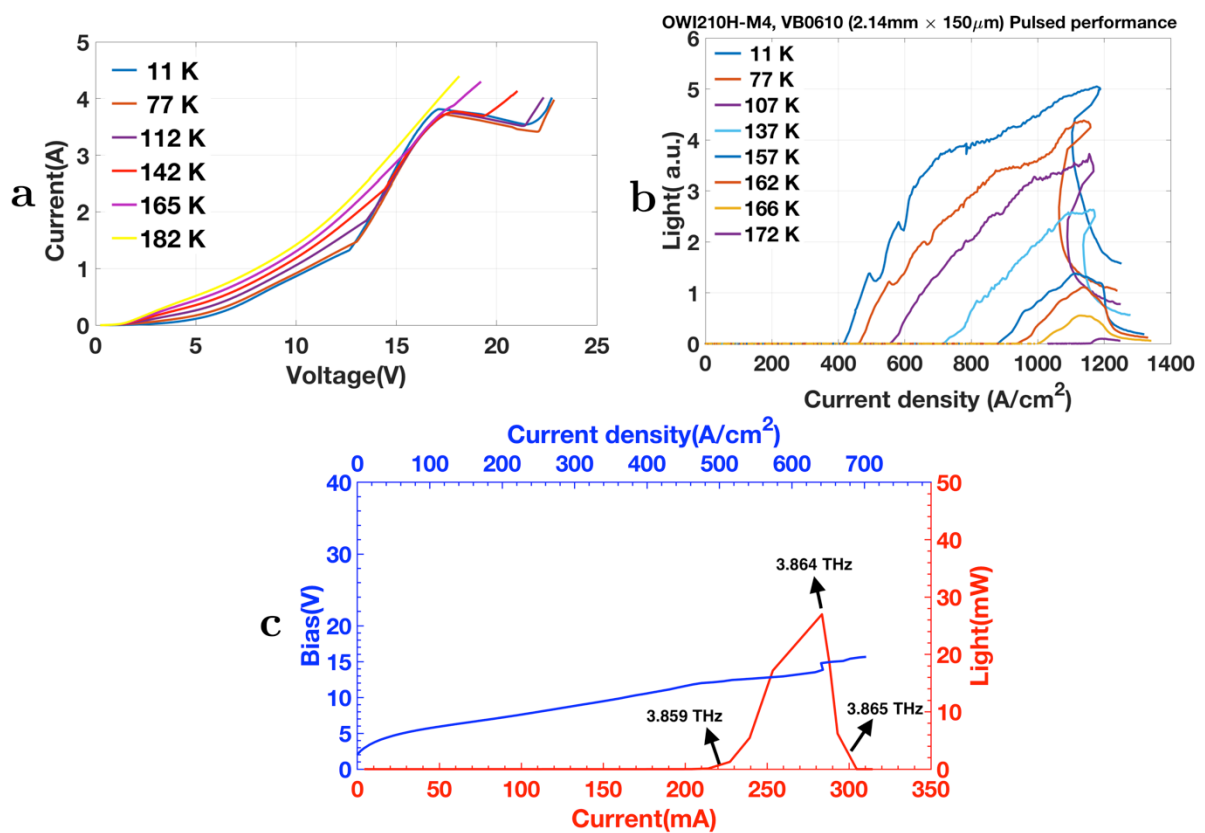

Figure S3: a, Current-Voltage at different temperatures for a FP device b, Light-Current at different temperatures for a FP device c, Light-Current-Voltage for a single ADFB.

π-coupled ADFBs with higher slope efficiency

In the main text, we have used a gain medium with a large Stark shift to achieve maximum frequency tuning. However, this gain medium has a high lasing current threshold which reduces its slope efficiency. We also tested a similar gain medium but with a lower doping so that the lasing threshold decreases. Figure S4 shows the characteristics of 5 π-coupled ADFBs made from this gain medium. 71 mW of CW power with 165 mW/A slope

efficiency is obtained. The Full Half Beam Width (FHBW) of $6^0 \times 8^0$ is achieved due to a perfect phase matching and a higher number of coupled ADFBs. The characteristic of single ADFB made from this gain medium is well characterized in reference[2]. More details on both gain media are given in reference[3].
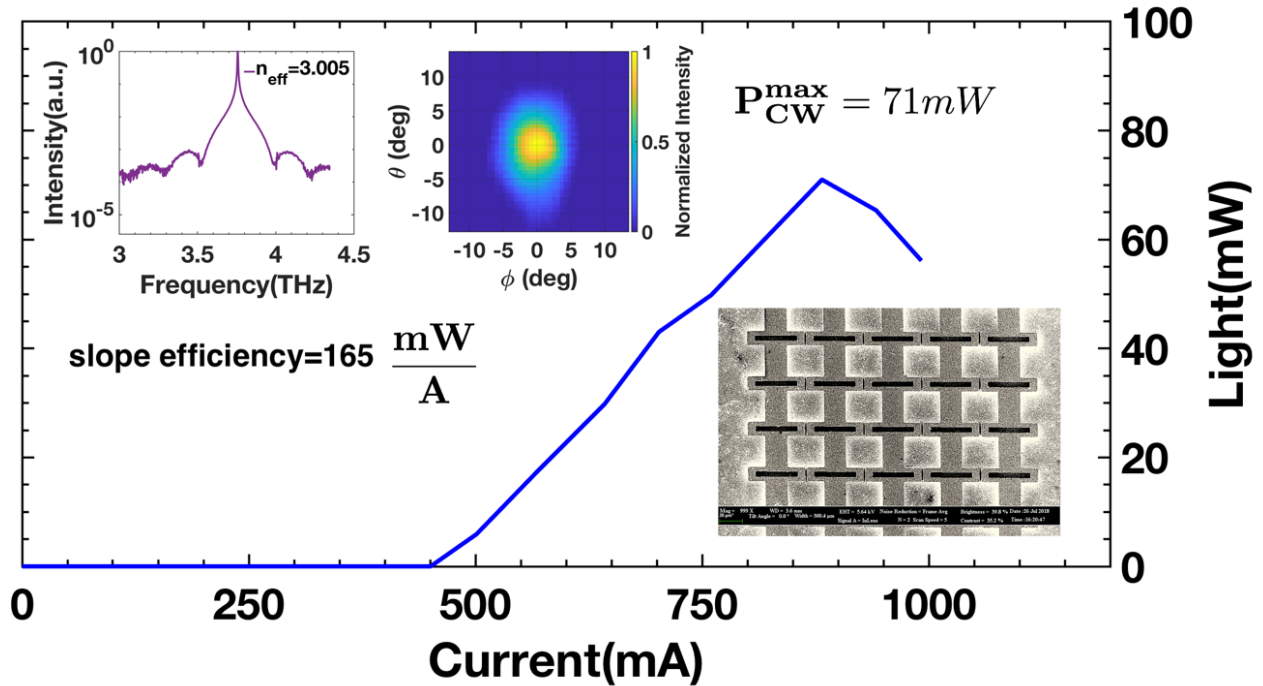

Figure S4: 5 stages π-coupled ADFBs fabricated on an active medium with lower current threshold (OWI210-VB605)

π-coupled ADFBs with larger antenna loop tip distance

In a different frequency range, we tried the same idea for 3 π-coupled unidirectional ADFBs[2]. The presence of reflector in such design limits how close the antenna loop tips could be. In one attempt, the distance from antenna loop tips was 10 μm. Figure S5 shows the spectrum from such a device.
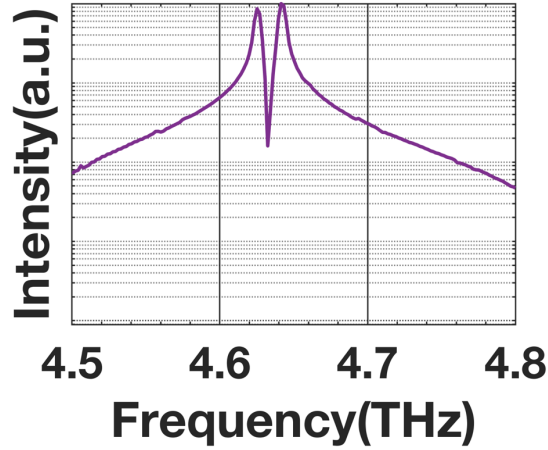
Figure S5: 3 stages π-coupled unidirectional ADFBs at 4.7 THz with 10-μm distances between antenna loop tips

Two peaks in the spectrum with about 20 GHz spacing were observed. We attributed the dual peaks to the symmetric and asymmetric modes, which are well matched with our simulation result. As shown in Figure1 in the main text, the closer the distance between antenna loop tips is, the higher selectivity can be achieved between the symmetric and asymmetric modes. Clearly, at this distance, the selectivity is so low that both modes are lasing.

Extra details for beat-note measurement

The free running beatnote was measured in heterodyne scheme to accurately measure the frequency tuning range (typical FTIR resolution of ~3 GHz is not sufficient for such experiment). The Schottky mixer is integrated with a horn antenna and a Bias-Tee box. The horn antenna aperture size is ~500 μm × 500 μm. The beam from the π-coupled ADFBs and the reference laser were focused on the Schottky mixer input RF/LO port (horn antenna aperture, marked 1 in figure S6). The focusing was achieved using two off-axis paraboloid mirrors. The IF output port, which contains the beatnote signal between the reference laser and the π-coupled ADFBs (port 2 marked in figure S6), was connected to a low-noise amplifier with 50-dB gain. The output of the low-noise amplifier was connected to a spectrum analyzer. The free running beatnote has a variation range about 50 MHz due to thermal fluctuation and mechanical vibration. (we did not phase lock the reference laser and the coupled ADFBs due to a negligible variation relative to the frequency difference ~ GHz).

The resolution bandwidth of spectrum analyzer was set to 1 MHz for high SNR. The video response monitor port yields the power detected by the mixer. It is worth mentioning that, due to a very sensitive beam alignment to such a small aperture of the integrated horn antenna, any instability in far field beam pattern of the lasers can be easily detected. Even though we did not measure the beam pattern at every bias point, the strong beatnote along the path provided in Figure 4 in the main text indicates the stability of the far-field beam pattern at different bias points.
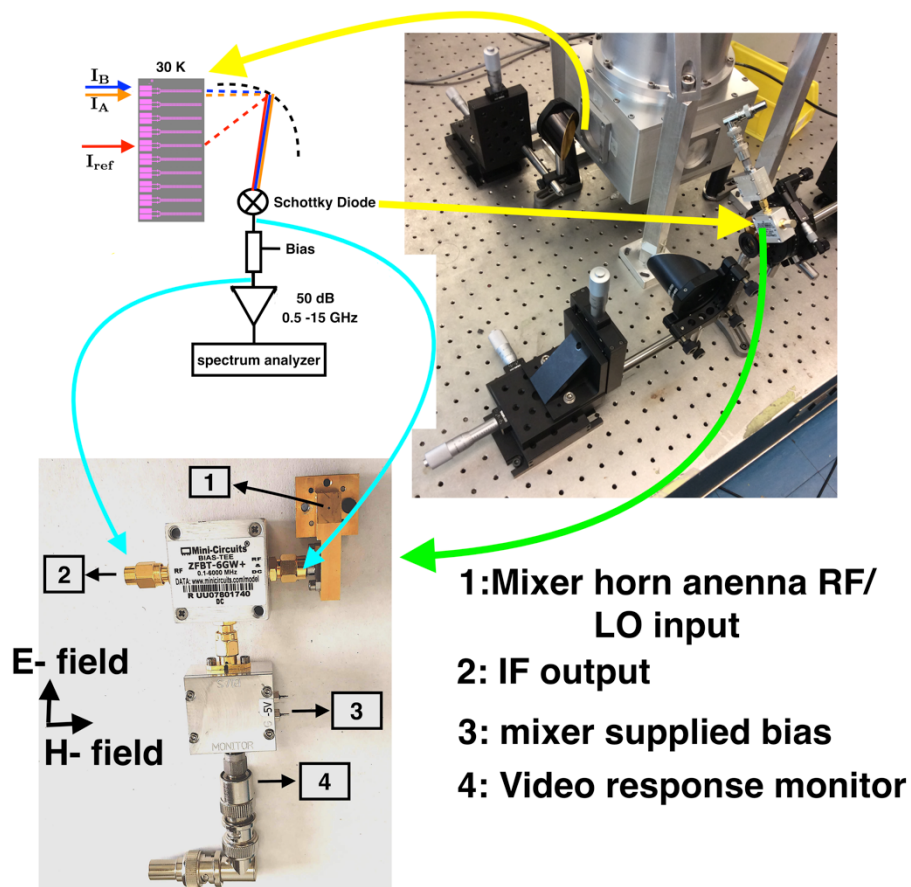

Figure S6: Set-up of heterodyne mixing to measure the frequency tuning range (no connecting wires are shown)

References

1. Bhattacharya, I., Chan, C. & Hu, Q. Effects of stimulated emission on transport in terahertz quantum cascade lasers based on diagonal designs. *Applied Physics Letters* **100**, 011108 (2012).
2. Khalatpour, A., Reno, J. L., Kherani, N. P. & Hu, Q. Unidirectional photonic wire laser. *Nature Photonics* **11**, 555 (2017).
3. Chan, C. W. I., Albo, A., Hu, Q. & Reno, J. L. Tradeoffs between oscillator strength and lifetime in terahertz quantum cascade lasers. *Applied Physics Letters* **109**, 201104 (2016).